Applied Mathematical Modelling 88 (2020) 38–54

Contents lists available at ScienceDirect

Applied Mathematical Modelling

journal homepage: www.elsevier.com/locate/apm

A stochastic method to account for the ambient turbulence in Lagrangian Vortex computations

Camille Choma Bex[a,b], Clément Carlier[a,b], Arnaud Fur[a,b], Grégory Pinon[a,*], Grégory Germain[b], Élie Rivoalen[c]

[a] Normandie Univ, UNILEHAVRE, CNRS, LOMC, 76600 Le Havre, France
[b] IFREMER, Institut Français pour la Recherche et l'Exploitation de la Mer Boulogne-Sur-Mer, France
[c] Normandie Univ, INSA Rouen, LMN, 76000 Rouen, France

ARTICLE INFO

Article history:
Received 6 July 2019
Revised 7 April 2020
Accepted 31 May 2020
Available online 17 June 2020

Keywords:
Ambient turbulence
Synthetic Eddy Method
Lagrangian method
Turbulence
Vortex method
Wake

ABSTRACT

This paper describes a detailed implementation of the Synthetic Eddy Method (SEM) initially presented in Jarrin et al. (2006) applied to the Lagrangian Vortex simulation. While the treatment of turbulent diffusion is already extensively covered in scientific literature, this is one of the first attempts to represent ambient turbulence in a fully Lagrangian framework. This implementation is well suited to the integration of PSE (Particle Strength Exchange) or DVM (Diffusion Velocity Method), often used to account for molecular and turbulent diffusion in Lagrangian simulations. The adaptation and implementation of the SEM into a Lagrangian method using the PSE diffusion model is presented, and the turbulent velocity fields produced by this method are then analysed. In this adaptation, SEM turbulent structures are simply advected, without stretching or diffusion of their own, over the flow domain. This implementation proves its ability to produce turbulent velocity fields in accordance with any desired turbulent flow parameters. As the SEM is a purely mathematical and stochastic model, turbulent spectra and turbulent length scales are also investigated. With the addition of variation in the turbulent structures sizes, a satisfying representation of turbulent spectra is recovered, and a linear relation is obtained between the turbulent structures sizes and the Taylor macroscale. Lastly, the model is applied to the computation of a tidal turbine wake for different ambient turbulence levels, demonstrating the ability of this new implementation to emulate experimentally observed tendencies.

1. Introduction

This paper deals with the simulation of ambient turbulence in the framework of the Lagrangian Vortex. Simulation of turbulence is among the most active current research topics as many problems remain unresolved, even with the increase of computational capacities. RANS (Reynolds Average Navier-Stokes), and its unsteady version U-RANS, LES (Large Eddy Simulation) and DNS (Direct Numerical Simulation) are the most frequent approaches to this problem in the Eulerian framework. DNS does not assume any model and therefore is the most reliable method, but its CPU time costs are incredibly high.

* Corresponding author.
E-mail addresses: camille.choma.bex@ifremer.fr (C. Choma Bex), gregory.pinon@univ-lehavre.fr (G. Pinon), gregory.germain@ifremer.fr (G. Germain), elie.rivoalen@insa-rouen.fr (É. Rivoalen).

https://doi.org/10.1016/j.apm.2020.05.025
0307-904X/

For the present engineering applications, LES is one of the most popular implementations as it allows the computation of relatively complex and large configurations within a reasonable CPU time. Sagaut [1] presents a review of the different procedures commonly used for Large Eddy Simulation. This LES approach is also possible in the Lagrangian framework: some researchers [2–4] have already carried out LES computations using the Lagrangian Vortex Method. In their last configuration, Mansfield et al. [4] computed a 3D vortex ring collision. Although these computations assessed the influence of turbulence, no ambient turbulence could be taken into account with this approach.

However, in many industrial applications, the ambient turbulence intensity in the upstream flow plays a determining role. This is especially the case in the fields of wind or tidal energy, the latter of which is considered in the present document. Velocity fluctuations induced by ambient turbulence have an impact not only on the performances of an individual turbine, but also on the shape and length of its wake. This is of utmost importance in the design of turbine arrays, when considering the effect of a row of upstream turbines on the power output of any turbines positioned downstream. Experimental studies in potential tidal sites show that this turbulence intensity can range from approximately 3% to 20% [5,6]. This percentage is calculated from the diagonal components of the Reynolds shear stress tensor and represents a characteristic percentage of the fluctuating velocity component with respect to the averaged incoming velocity field. Such non-negligible variations in inflow conditions must be taken into account when attempting to replicate numerically the true operating conditions of a tidal turbine.

Therefore, various methods have been developed to emulate the ambient turbulence in the context of Eulerian simulations, through the use of boundary conditions. The Synthetic Eddy Method (SEM) proposed by Jarrin et al. [7,8] was initially formulated within this context: its original purpose is to generate inflow conditions for the Eulerian simulation of turbulent flows. Jarrin et al. [7] defined a set of turbulent structures to represent a desired fluctuating velocity field at the inlet of their computational domain. This approach was already used by several authors such as Afgan et al. [9], or Ahmed et al. [10]. As for marine current turbine simulations, Togneri et al. [11,12] investigated a similar Synthetic Eddy Method in order to generate synthetic turbulent inflow conditions for their BEMT software. Others use the TurbSim generator from NREL [13] which generates the desired turbulent inflow conditions from a spectral representation of turbulence. For instance, Churchfield et al. [14] used TurbSim to generate inflow conditions for their tidal turbine farm computations. Togneri et al. [15,16] compare the SEM and spectral based turbulent inflow generation methods in order to investigate fluctuations in loads on the turbine, using their BEMT code. Lastly, Mann's algorithm [17] is another similar approach based on spectral representation of turbulence. Chatelain et al. [18,19] used this algorithm to generate a turbulent inflows for wind turbines simulations. The numerical method used by Chatelain et al. [18,19] is a particle-mesh method relying on an Eulerian mesh at some steps of the numerical scheme, which allows turbulent flow states to be used as inflow boundary conditions. All these cited approaches share the complication of their difficulty to maintain the chosen inflow ambient turbulence intensity level throughout the whole flow domain. As mentioned by Jarrin et al. [7,8], the ambient turbulence intensity usually decreases as the flow progresses, and the desired input level is generally not recovered in the area of interest of the computational domain.

None of these above mentioned methods can be applied as such to a pure Lagrangian Vortex framework, and the adaptation of one of them is the topic of the present paper. Our numerical model represents the vortical flow field by means of a set of Lagrangian Vortex particles and the velocity field is obtained via the Biot & Savart equation. This paper presents an adaptation of the initial SEM method of Jarrin et al. which maintains the turbulence intensity level over the entire flow domain, ensured by the advection of turbulent structures with no stretching or diffusion. This can be of major importance for the simulation of wind or tidal turbine farms, to ensure that turbines perceive similar levels of turbulent intensity throughout the entire farm area and all the way downstream to the last row of turbines. Additionally the method presented here can function together with both of the most common treatments of diffusion in Lagrangian Vortex methods, namely the Particle Strength Exchange (PSE) [20–22] and the Diffusion Velocity Method (DVM) [23]. These methods can integrate turbulent diffusion models, such as Large Eddy Simulation [2–4,24], to better represent all turbulent length scales.

First of all, an overview is given of the unsteady Lagrangian method, and its treatment of the diffusion is further detailed. The adapted SEM is then presented and analysed on a simple study case. Finally the combination of adapted SEM and Vortex methods is applied to the simulation of a simplified marine current turbine in varying turbulent conditions.

2. Ambient turbulence model in the Lagrangian framework

As a matter of nomenclature convention, bold signs will refer to vectors, regular letters will refer to continuous fields (*e.g.* $\boldsymbol{u}$ for the continuous velocity field) and capital letters will refer to the corresponding discretised field (*e.g.* $\boldsymbol{U}_i$ for for the velocity of the i-th particle).

This Section covers the Vortex method used for the simulation of marine current turbines and their wakes, as well as the integration of a Synthetic Eddy Method adapted to the context of these computations.

2.1. Lagrangian Vortex method and treatment of diffusion

The Vortex method is an unsteady Lagrangian method, based on a discretisation of the flow into vorticity carrying particles [22,25–27]. The governing equations for this unsteady and incompressible flow are the Navier-Stokes equations in their

velocity/vorticity ($\boldsymbol{u}$, $\boldsymbol{\omega}$) formulation:

$$\nabla \cdot \boldsymbol{u} = 0, \tag{1}$$

$$\frac{D\boldsymbol{\omega}}{Dt} = (\boldsymbol{\omega} \cdot \nabla)\boldsymbol{u} + \nu \Delta \boldsymbol{\omega}, \tag{2}$$

where $\boldsymbol{u}$ is the velocity field, $\boldsymbol{\omega} = \nabla \wedge \boldsymbol{u}$ is the vorticity field and ν is the kinematic viscosity. Eq. (2) is the momentum equation transposed into the velocity-vorticty formulation, with $(\boldsymbol{\omega} \cdot \nabla)\boldsymbol{u}$ representing the stretching term and $\nu \Delta \boldsymbol{\omega}$ the diffusion term. The fluid domain is discretised into N particles, each particle i represented by its position $\boldsymbol{X}_i$, its vortical weight $\boldsymbol{\Omega}_i$, and its volume $\mathcal{V}_i$. The particles' transport over time is described by the following displacement equation, integrated using regular time stepping schemes:

$$\frac{\mathrm{d}\boldsymbol{X}_i}{\mathrm{d}t} = \boldsymbol{u}(\boldsymbol{X}_i) = \boldsymbol{U}_i. \tag{3}$$

This leads to a discretised formulation of the previous Navier-Stokes Eq. (2), dictating the evolution of the vorticity carried by each particle i:

$$\frac{\mathrm{d}\boldsymbol{\Omega}_i}{\mathrm{d}t} = \underbrace{(\boldsymbol{\Omega}_i \cdot \nabla)\boldsymbol{U}_i}_{\text{Stretching term: } \mathcal{S}_i\mathcal{V}_i} + \underbrace{\nu[\Delta\boldsymbol{\omega}]_{\boldsymbol{x}=\boldsymbol{X}_i}\mathcal{V}_i}_{\text{Diffusion term: } \mathcal{L}_i\mathcal{V}_i} \tag{4}$$

For an explanation of the treatment of the stretching term $\mathcal{S}_i\mathcal{V}_i$, the reader is referred to Cottet and Koumoutsakos [22].

The Lagrangian Vortex method is based on a Helmholtz decomposition of the velocity field:

$$\boldsymbol{U} = \underbrace{\nabla \wedge \boldsymbol{\psi}}_{\boldsymbol{U}^{\psi}} + \underbrace{\nabla \phi}_{\boldsymbol{U}^{\phi}} + \boldsymbol{U}^{\infty}, \tag{5}$$

where the components of the velocity can be detailed as the following:

- A rotational velocity component $\boldsymbol{U}^{\psi}$ accounting for particle-particle interaction, the core of any Lagrangian Vortex method. This component $\boldsymbol{U}^{\psi}$ is the discrete solution of the continuous equation:

  $$\Delta \boldsymbol{\psi} = -\boldsymbol{\omega}, \tag{6}$$

  obtained by introducing the Helmholtz decomposition (Eq. (5)) into the definition of vorticity. The solution for this Eq. (6) is given at any point M of the fluid domain by the Biot & Savart law [22,25,28,29]:

  $$\boldsymbol{U}^{\psi}(M) = \frac{1}{4\pi} \sum_{i=1}^{N} \frac{\boldsymbol{M}\boldsymbol{X}_i}{|\boldsymbol{M}\boldsymbol{X}_i|^3} \wedge \boldsymbol{\Omega}_i. \tag{7}$$

  This formulation is desingularised using a regularisation parameter ϵ, as described by Winckelmans and Leonard [29]. Additional developments are carried out in the numerical implementation of this formulation, such as a *Treecode* type acceleration algorithm (see Lindsay and Krasny [30]) and remeshing algorithms (see Cottet and Koumoutsakos [22]), as well as time stepping procedures.
- A potential velocity component $\boldsymbol{U}^{\phi}$, representing the influence of a solid body. There are many applications for the use of such a component, such as the simulation of the nozzle of jet [31], of a sail [32], or of a monofin [33]. In the present study, the potential velocity component represents the influence of the rotor of a turbine [27], as will be demonstrated in Section 4. This velocity component $\boldsymbol{U}^{\phi}$ derives from a scalar potential ϕ, which must satisfy:

  $$\Delta \phi = 0. \tag{8}$$

  Eq. (8) is obtained by introducing the velocity decomposition equation (5) into the continuity equation (1). The latest developments on this aspect of the software are detailed by Carlier et al. [34] as well as Mycek et al. [35].
- A velocity component $\boldsymbol{U}^{\infty}$ representing the upstream velocity field at infinity, generally treated as a constant vector.

The focus of this paper is to adapt the upstream velocity component $\boldsymbol{U}^{\infty}$ in order to account for ambient turbulence in the surrounding flow. Before these latest developments are presented, the following paragraphs recall the treatment of diffusion in the Lagrangian framework, along with the LES approach.

When considering a viscous fluid with a constant viscosity ν, the diffusion term $\mathcal{L}_i\mathcal{V}_i$ from Eq. (2) is described in accordance with the Particle Strength Exchange method initially developed by Degond and Mas-Gallic [20] and Choquin and Huberson [21]:

$$\mathcal{L}_i\mathcal{V}_i = \nu[\Delta\boldsymbol{\omega}]_{\boldsymbol{x}=\boldsymbol{X}_i}\mathcal{V}_i \simeq \nu \sum_{j=1}^{N} \left[\boldsymbol{\Omega}_j\mathcal{V}_i - \boldsymbol{\Omega}_i\mathcal{V}_j\right] \eta_{\epsilon}^{\mathrm{lap}}\left(\boldsymbol{X}_i - \boldsymbol{X}_j\right), \tag{9}$$

where $\eta_\epsilon^{\text{lap}}$ is a regularised kernel built in order to approximate the three dimensional Laplacian operator. In the present study, $\eta_\epsilon^{\text{lap}}$ is defined as:

$$\eta_\epsilon^{\text{lap}}(\boldsymbol{x}) = \frac{1}{\epsilon^3}\eta^{\text{lap}}\left(\frac{\boldsymbol{x}}{\epsilon}\right), \tag{10}$$

with η^{lap} a second order Gaussian kernel:

$$\eta^{\text{lap}}(\boldsymbol{x}) = \frac{4}{\epsilon^2\pi^{3/2}}\exp\left(-|\boldsymbol{x}|^2\right). \tag{11}$$

When developing a method to account for ambient turbulence in the surrounding flow, it becomes all the more important to account for turbulent diffusion among the Vortex particles. This is accomplished via the use of a Large Eddy Simulation model, in order to represent the influence of the non-resolved length scales. LES models are based on the definition of an eddy viscosity ν_T, which is usually not constant. The diffusion term $\boldsymbol{\mathcal{L}}_i\mathcal{V}_i$ of Eq. (9) becomes:

$$\boldsymbol{\mathcal{L}}_i\mathcal{V}_i = \left[(\nu+\nu_T)\Delta\boldsymbol{\omega} + (\boldsymbol{\nabla}\nu_T)\wedge(\Delta\boldsymbol{u})\right]_{\boldsymbol{x}=\boldsymbol{X}_i}\mathcal{V}_i. \tag{12}$$

Several expressions exist for the eddy viscosity ν_T, among which can be cited those of Smagorinsky (as described by Sagaut [1]), Mansfield et al. [4,36], and Mansour [37]. Sagaut [1] has assembled a synthetic analysis of these various formulations. In the present study, the turbulent eddy viscosity is computed as defined by Mansour [37]:

$$\nu_T = (C_M\Delta)^2\sqrt{2}|\boldsymbol{\omega}|, \tag{13}$$

where C_M is a constant to be fixed (in the present case at $C_M = 0.2$), and Δ is the average distance between particles. Thus, the turbulent eddy viscosity $\nu_{T,i}$ of for the i^{th}-particle can be expressed as:

$$\nu_{T,i} = \nu_T(\boldsymbol{X}_i) \simeq (C_M\Delta)^2\sqrt{2}\frac{|\boldsymbol{\Omega}_i|}{\mathcal{V}_i}. \tag{14}$$

An alternative numerical approach for diffusion is possible in the Lagrangian Vortex framework: the Diffusion Velocity Method (DVM), initially proposed by Ogami and Akamatsu [23] and recently analysed by Mycek et al. [24]. This last study also offers some perspective on the three-dimensional treatment of diffusion with LES using a DVM approach [24].

2.2. Synthetic Eddy Method for simulating ambient turbulence

The aim of this study is to account for ambient turbulence in the fluid, with any given turbulence parameters and at any point in the study space. The Synthetic Eddy Method formulated by Jarrin et al. [7,8] allows the generation of an input flow with any given turbulent intensity I_∞ and anisotropic ratio (σ_u:σ_v:σ_w). Within Jarrin's initial formulation, these turbulence conditions are only verified at the inlet of the fluid domain. In the present study, this method is adapted in order to cover the entirety of a given study space. The ambient turbulence intensity percentage I_∞ quantifies the velocity fluctuations in a three-dimensional flow $(u_\infty, v_\infty, w_\infty)$ as the following:

$$I_\infty = 100\sqrt{\frac{\frac{1}{3}\left[\sigma^2(u_\infty)+\sigma^2(v_\infty)+\sigma^2(w_\infty)\right]}{\bar{u}_\infty^2+\bar{v}_\infty^2+\bar{w}_\infty^2}} \tag{15}$$

In the Synthetic Eddy Method proposed by Jarrin, ambient turbulence in the upstream flow is accounted for by modifying the upstream velocity component $\boldsymbol{u}^\infty$. This upstream velocity is rewritten via the Reynolds decomposition:

$$\boldsymbol{u}^\infty(\boldsymbol{x}) = \overline{\boldsymbol{u}^\infty} + \tilde{\boldsymbol{u}}(\boldsymbol{x}) \tag{16}$$

where $\overline{\boldsymbol{u}^\infty}$ is the mean velocity of the flow and $\tilde{\boldsymbol{u}}$ a perturbation term encompassing the fluctuations due to ambient turbulence. The perturbation term $\tilde{\boldsymbol{u}}$ is calculated as the influence of N "turbulent structures", also called "eddies", randomly positioned throughout a three-dimensional study space of volume $\tilde{V}$. Each "turbulent structure" k is characterized by its position $\boldsymbol{x}^k$ and its intensity $\boldsymbol{c}^k$, defined in the following paragraphs. The perturbation induced by N turbulent structures is computed as the sum of the influences of each structure k:

$$\tilde{\boldsymbol{u}}(\boldsymbol{x}) = \sum_{k=1}^{N}\tilde{\boldsymbol{u}}^k(\boldsymbol{x}), \tag{17}$$

with $\boldsymbol{x}$ a point of the fluid domain and $\tilde{\boldsymbol{u}}^k$ the perturbation velocity induced by a single turbulent structure k. This individual perturbation velocity is expressed as:

$$\tilde{\boldsymbol{u}}^k(\boldsymbol{x}) = \sqrt{\frac{\tilde{V}}{N}}\boldsymbol{c}^k F_{\boldsymbol{\lambda}}(\boldsymbol{x}-\boldsymbol{x}^k) \quad \forall k \in [\![1,N]\!], \tag{18}$$

where $F_{\boldsymbol{\lambda}}$ is a shape function, discussed further below. As for the intensity $\boldsymbol{c}^k$, its three components are defined as:

$$c_i^k = \sum_{j=1}^{3} a_{i,j}\epsilon_{i,j}^k \quad \forall i \in \{1,2,3\}, \quad \forall k \in [\![1,N]\!]. \tag{19}$$

All instances of $\epsilon_{i,j}^k$ are random sign variables of values of 1 or -1, representing the random aspect of turbulence. The terms $a_{i,j}$ are the elements of the Cholesky decomposition matrix A of the Reynolds Stress Tensor $\overline{\overline{\boldsymbol{R}}}$:

$$\overline{\overline{\boldsymbol{R}}} = \begin{pmatrix} R_{1,1} & R_{1,2} & R_{1,3} \\ R_{2,1} & R_{2,2} & R_{2,3} \\ R_{3,1} & R_{3,2} & R_{3,3} \end{pmatrix} = \overline{\overline{\boldsymbol{A}}}\,\overline{\overline{\boldsymbol{A}}}^T \quad \text{with} \quad \overline{\overline{\boldsymbol{A}}} = \left(a_{i,j}\right) \tag{20}$$

Through Eqs. (19) and (20), the link between the intensities $\boldsymbol{c}^k$ of the turbulent structures and the Reynolds Stress Tensor $\overline{\overline{\boldsymbol{R}}}$ ensures the generation of a velocity field that statistically replicates any given turbulence intensity I_∞ and any given anisotropic ratio $(\sigma_u{:}\sigma_v{:}\sigma_w)$ [7,38]. Indeed the three components of the anisotropic ratio $(\sigma_u{:}\sigma_v{:}\sigma_w)$ are given by the square roots of the diagonal components of the Reynolds Stress Tensor $\overline{\overline{\boldsymbol{R}}}$. Moreover the turbulent intensity I_∞ can be rewritten as a function of the trace of the Reynolds Stress Tensor $\overline{\overline{\boldsymbol{R}}}$:

$$\begin{aligned} I_\infty &= 100\sqrt{\frac{1/3\left[\sigma^2(u_\infty)+\sigma^2(v_\infty)+\sigma^2(w_\infty)\right]}{\bar{u}_\infty^2+\bar{v}_\infty^2+\bar{w}_\infty^2}} \\ &= \frac{100}{|\boldsymbol{u}^\infty|}\sqrt{\frac{R_{1,1}+R_{2,2}+R_{3,3}}{3}} \\ &= \frac{100}{|\boldsymbol{u}^\infty|}\sqrt{\frac{\mathbf{tr}\left(\overline{\overline{\boldsymbol{R}}}\right)}{3}} \end{aligned} \tag{21}$$

This last Eq. (21) ensures that the turbulent field will have the desired turbulent intensity I_∞ and anisotropic ratio $(\sigma_u{:}\sigma_v{:}\sigma_w)$.

The shape function $F_{\boldsymbol{\lambda}}$ appearing in Eq. (18) is defined as prescribed by Jarrin et al.:

$$F_{\boldsymbol{\lambda}}(\boldsymbol{y}) = \prod_{i=1}^{3} f_{\lambda_i}(y_i). \tag{22}$$

$\boldsymbol{\lambda}$ determines the size of the area of influence of each turbulent structure k. This size could be interpreted naively as a turbulent length scale (such as the Taylor or Kolmogorov length scales), but its implementation is not as straightforward. The structure sizes $\boldsymbol{\lambda}$ are a user-defined parameter which can be chosen based on characteristics of the turbulent flow which is to be reproduced. Additional information on the choice of the parameter $\boldsymbol{\lambda}$ can be found in the following Section 3.2. The fact the $\boldsymbol{\lambda}$ is defined as a vector allows the area of influence to have different sizes λ_i in each direction i. Each individual turbulent structure k could also have its own vector size $\boldsymbol{\lambda}_k$, as will also be discussed in the following Sections. The sub-function f_λ used in the evaluation of the shape function $F_{\boldsymbol{\lambda}}$ must meet certain requirements in order to ensure that the ambient turbulence is generated with the chosen characteristics:

$$\underset{y}{\operatorname{argmax}}(f_\lambda(y)) = 0, \tag{23a}$$

$$f_\lambda(y) = f_\lambda(-y), \tag{23b}$$

$$\int_{-\lambda}^{\lambda} f_\lambda^2(y)dy = 1. \tag{23c}$$

These three Eqs. (23a), (23b) and (23c) are of crucial importance to the proper functioning of the numerical model.

For the preliminary results presented in Section 3, a basic shape function $F_{\boldsymbol{\lambda}}$ given by Jarrin et al. is used. Its sub-function f_λ is a tent function, here a triangular function centered around zero with a base of 2λ:

$$f_\lambda(y) = \begin{cases} \sqrt{\dfrac{3}{2\lambda^3}}(\lambda - |y|) & \text{if} \quad |y| < \lambda \\ 0 & \text{otherwise.} \end{cases} \tag{24}$$

This basic tent function belongs to the C^0-class functions: it is continuous but its first derivative presents large discontinuities. In the framework of Lagrangian Vortex computations, such discontinuities in the velocity derivatives can be problematic, more specifically for the evaluation of the stretching term $\mathcal{S}_i\mathcal{V}$ as presented in Eq. (4). Following the conditions cited in Eqs. (23a) (23b) and (23c), smoother alternative shape functions f_λ can be defined. Three examples of class C^1 or more are considered:

- A sinusoidal shape function:

$$f_\lambda(y) = \begin{cases} \dfrac{1}{\sqrt{3\lambda}}\left(\cos(\dfrac{\pi}{\lambda}y)+1\right) & if \quad -\lambda \le y \le \lambda \\ 0 & otherwise \end{cases} \tag{25}$$

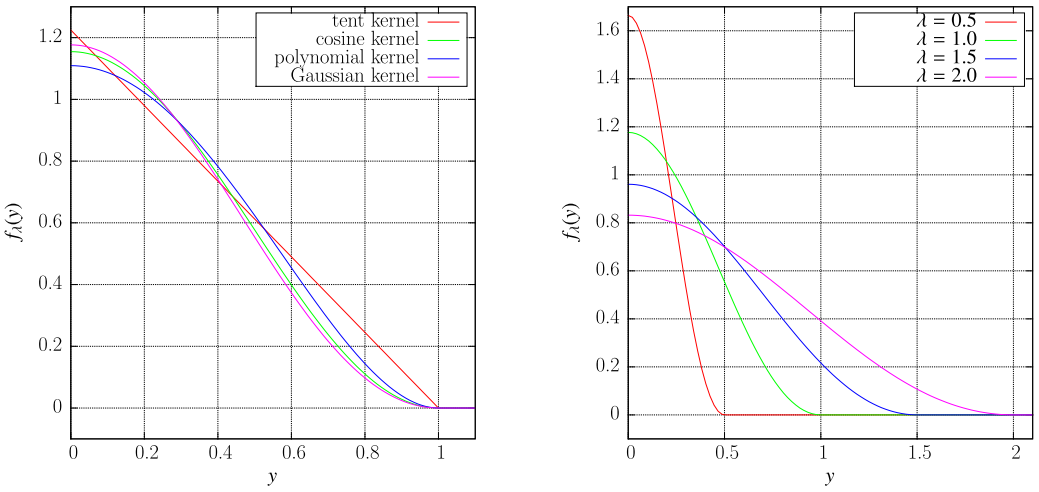

(a) Shape functions f_λ (b) Different sizes λ

Fig. 1. The four different kernels for $\lambda = 1$ and the Gaussian kernel for different sizes λ of turbulent structures.

- A polynomial shape function:

$$f_\lambda(y) = \begin{cases} \sqrt{\frac{315}{256\lambda}}\left(\frac{y^4}{\lambda^4} - \frac{2y^2}{\lambda^2} + 1\right) & if \ -\lambda \le y \le \lambda \\ 0 & otherwise \end{cases} \tag{26}$$

- A Gaussian shape function:

$$f_\lambda(y) = \begin{cases} c(\lambda)\left(1 - \frac{\exp(1)\ y^2}{\lambda^2}\exp\left(-\frac{y^2}{\lambda^2}\right)\right) & if \ -\lambda \le y \le \lambda \\ 0 & otherwise \end{cases} \tag{27}$$

where $c(\lambda) = \dfrac{1}{\sqrt{L\left(\frac{25}{8} + \frac{3\ \exp(2)\ \sqrt{\pi} * \mathrm{erf}(\sqrt{2})}{16\sqrt{2}} - \exp(1)\ \sqrt{\pi} * \mathrm{erf}(1)\right)}}$.

Fig. 1a depicts the four kernels for $\lambda = 1$, and Fig. 1b the Gaussian kernel for different values of λ.

Lastly, the theory of turbulent scales dictates that every turbulent flow contains a wide range of magnitudes of turbulent behavior. Despite its purely mathematical nature, the purpose of this model remains to best represent the true physical phenomenon of turbulent agitation. Thus a standard deviation of the size of turbulent structures, denoted $\sigma(\lambda)$, is added as a parameter of the model. At deviation zero, all turbulent structures k have the same size $\boldsymbol{\lambda}$. A non-zero value of deviation results in a term $\sigma(\lambda)$ being added into the size of each turbulent structure (independantly in each direction $i = 1, 2, 3$), generating turbulent structures ranging in size. The added term $\sigma(\lambda)$ is computed so as to ensure that these sizes are normally distributed around a certain average value: $\lambda \sim \mathcal{N}(\lambda,\ \sigma^2(\lambda))$, as illustrated in Fig. 2. The standard deviation $\sigma(\lambda)$ is expressed as a percentage of the variable λ, for instance: $\sigma(\lambda) = 10\% = 0.1\ \lambda$. In all cases, this results in a more or less wide spread of turbulent structure sizes, centered around the average given by the initially prescribed values of $\boldsymbol{\lambda}$.

If the normal law is not limited, λ could potentially reach negative values, which has no physical meaning. With a heightened value of the standard deviation, it could also lead to the generation of structures of abnormally large size. To solve this problem, boundaries are introduced to the values that λ can take within the prescribed standard deviation. A lower boundary ensures that the size of the turbulent structures can only be positive, while an upper boundary restricts these sizes to under twice the prescribed average value. If the randomly generated size does not meet these criteria, i.e if $\lambda \notin\ ]0;\ 2\lambda]$, it is not taken into account and a new structure size is generated. This upper boundary was selected so that the average size of all structures remains substantially equal to the prescribed value λ.

2.3. Integration of the Synthetic Eddy Method into the Vortex method

The Vortex Particle Method is an unsteady Lagrangian method in an unbounded domain, where the fluid domain is considered to be infinite. However as mentioned previously, the Synthetic Eddy Method requires the definition of a set volume $\tilde{V}$ containing all the turbulent structures, defined as the volume of a box-shaped space $\tilde{E}$. A second space E_S is considered within $\tilde{E}$ as the actual area of interest inside which the ambient turbulence is desired. In order to obtain statistically correct

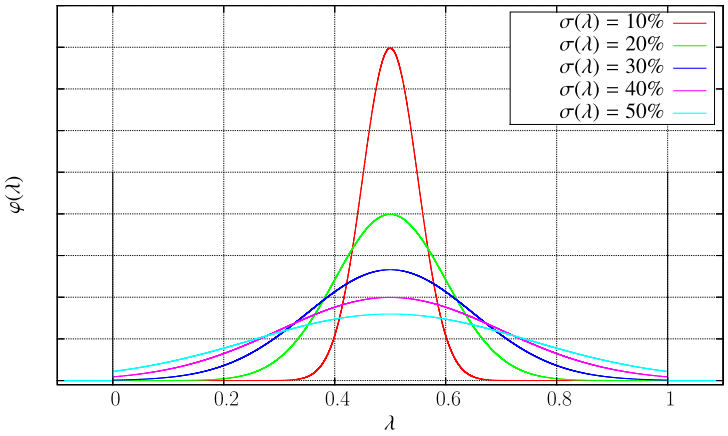

Fig. 2. Normal distributions centred around $\lambda = 0.5$.

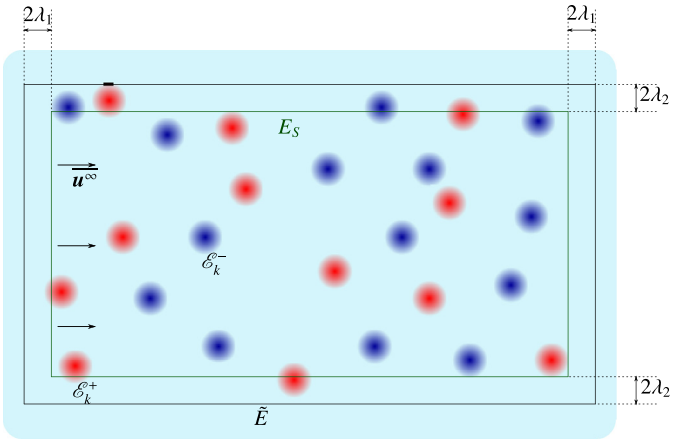

Fig. 3. Schematic view of the integration of the Synthetic-Eddy-Method into the Vortex method.

velocity fluctuations all over the study space E_S, enough buffering space must be left over between $\tilde{E}$ and E_S to ensure the uniformity of the fluctuations all over the area of interest. This can be written as the following conditions:

$$\min\left(x_i \in \tilde{E}\right) \leq \min\left(x_i \in E_S\right) - 2\lambda_i \quad \forall i \in \{1,2,3\}, \tag{28a}$$

$$\max\left(x_i \in \tilde{E}\right) \geq \max\left(x_i \in E_S\right) + 2\lambda_i \quad \forall i \in \{1,2,3\} \tag{28b}$$

with $\boldsymbol{x}$ a position vector and $\boldsymbol{\lambda} = \lambda_i\,(i = 1,3)$ the size vector of the turbulent structures, as illustrated in Fig. 3. From this point onwards, in all subsequent Figures the flow direction is represented from the left to the right. The upstream velocity field $\overrightarrow{\boldsymbol{u}^{\infty}}$ is shown in the direction of the flow and applied throughout the entire domain E_S.

N turbulent structures k are generated within the chosen space $\tilde{E}$, at random initial positions and of sizes distributed around the average vector size $\boldsymbol{\lambda}$, as discussed in the previous Sub-Section. The saturation level of turbulent structures is described by a filling ratio R_f:

$$R_f = \sum_{k=1}^{N} \frac{V_k}{\tilde{V}} \tag{29}$$

where V_k is the volume of the area of influence of the structure k (i.e., $V_k = \frac{4}{3}\pi\lambda_1\lambda_2\lambda_3$).

The algorithmic procedure of the SEM progresses as such: each turbulent structure k is characterized at the moment of its generation by an intensity $\boldsymbol{c}^k$ calculated using Eq. (19), and a random value $\epsilon_{i,j}^k$ with equal probabilities of being 1 or -1. After their initialization, the turbulent structures are advected with the flow as the simulation proceeds. If during the course of the simulation a turbulent structure is advected outside of the boundaries of the space $\tilde{E}$, it is deleted, and replaced by a newly generated structure at the inlet of the space, *i.e.* the leftmost boundary of the schematic representation of Fig. 3.

Different strategies can be considered for the advection of turbulent structures, with varying levels of coupling and complexity. First of all, the structures can be advected either with the constant average upstream velocity $\overrightarrow{\boldsymbol{u}^{\infty}}$ or with the

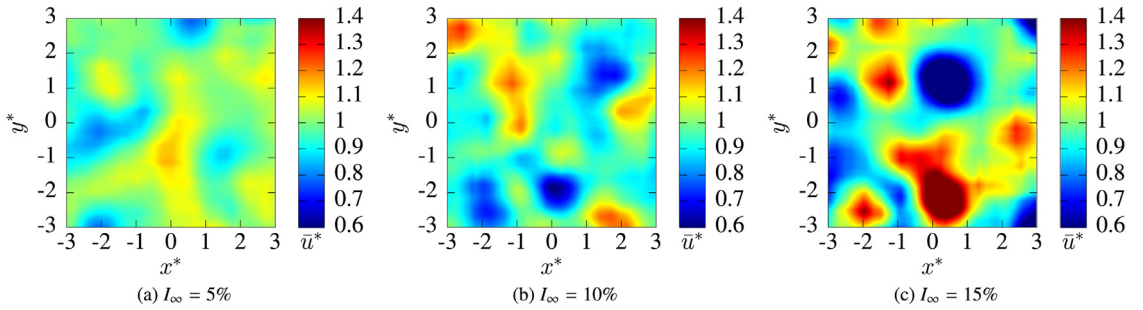

Fig. 4. Examples of velocity fields provided by the Syntehtic Eddy model for $N = 1000$ structures of fixed size $\lambda = 1$ ($R_f = 19.4$) and different values of I_∞. Slice at $z = 0$ of the 3D reconstructed velocity field of size $6 \times 6 \times 6$.

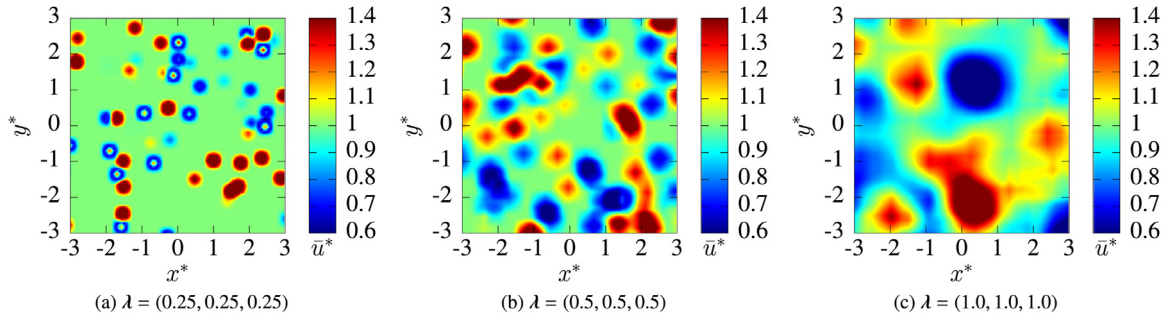

Fig. 5. Example of velocity fields provided by the Synthetic Eddy model for $I_\infty = 15\%$, $N = 1000$ structures and different structure sizes ($R_f = 0.3$, 2.4 and 19.4 respectively). Slice at $z = 0$ of the 3D reconstructed velocity field of size $6 \times 6 \times 6$.

complete flow velocity $\boldsymbol{u}$, as defined in Eq. (5). However, if the structures were to be advected with the flow velocity $\boldsymbol{u}$, several questions would arise. As the validity of the Synthetic Eddy Method relies on the randomness of the locations of the turbulent structures, it is unclear whether this property would remain valid if the turbulent structures were advected with a non uniform velocity. Additional tests would need to be carried out in order to ensure that the Reynolds Stress Tensor is still satisfyingly replicated.

Secondly, the added turbulent velocity term $\tilde{\boldsymbol{u}}(\boldsymbol{x})$ could be included in the computation of the stretching and diffusive terms of the Navier-Stokes equation (first and second terms of the right side of Eq. (2)). In this preliminary study, the simplest options are selected: advecting the turbulent structures with the constant velocity $\overline{\boldsymbol{u}^\infty}$, and omitting their influence in the calculation of stretching and diffusive terms of the Navier-Stokes equation.

3. Numerical reconstruction of turbulent velocity fields

In order to study the turbulent flows generated by the Synthetic Eddy Method and the influence of its various parameters, numerically generated flows are investigated with basic inflow conditions. Throughout this section, unless stated otherwise the mean inflow velocity is chosen as $|\boldsymbol{U}^\infty| = 1\ m/s$, and the anisotropic ratio as $(\sigma_u : \sigma_v : \sigma_w) = (1 : 0.75 : 0.56)$ based on the observations of Milne et al. [5]. For ease of notation, when the average turbulent structure size vector $\boldsymbol{\lambda}$ has the same value in each direction $i = 1, 2, 3$, this size will be referred to as the single value λ (i.e. $\lambda_1 = \lambda_2 = \lambda_3 = \lambda$ or $\boldsymbol{\lambda} = (\lambda, \lambda, \lambda)$).

3.1. Analysis of the velocity fields

Fig. 4 shows examples of turbulent flow fields generated with the Synthetic-Eddy-Method for different values of turbulent intensity I_∞. At first glance, these flows appear to be very realistic, with the disruptions to the flow field increasing with the value of the turbulent intensity. The size of the turbulent structures, set to $\lambda = 1$, is not immediately apparent. Fig. 5 shows the influence of this size parameter, for a fixed value of the turbulent intensity and no variance on the structure sizes. When the turbulent structures are small, each structure can be clearly identified; whereas when the sizes increase, individual structure shapes are lost in the overlap. Fig. 6 shows the influence of anisotropy in the set value of turbulent structure sizes $\boldsymbol{\lambda}$, with no variance allowed. The outlined turbulent structures clearly take on a more elongated oval shape as prescribed by their dimensions. Fig. 7 shows the influence of the variation $\sigma(\lambda)$ allowed around the prescribed average turbulent structure sizes $\boldsymbol{\lambda}$. For higher variations $\sigma(\lambda)$, the shapes of the turbulent structures become increasingly eclectic and diverse, as these variations are independent in each dimension.

Beyond controlling the appearance of the turbulent velocity fields, the main function of the Synthetic Eddy Method is its ability to reproduce any given Reynolds Stress Tensor. This ensures the correct representation of any given turbulence

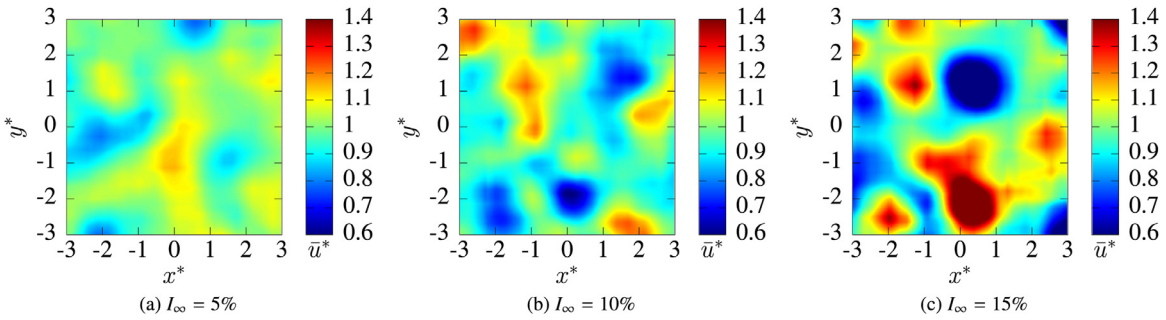

Fig. 6. Example of velocity field provided by the ambient turbulence model for $I_\infty = 15\%$, $N = 1000$ structures and different structure sizes ($R_f = 1.9$, 1.5 and 1.0 respectively). Slice at $z = 0$ of the 3D reconstructed velocity field of size $6 \times 6 \times 6$.

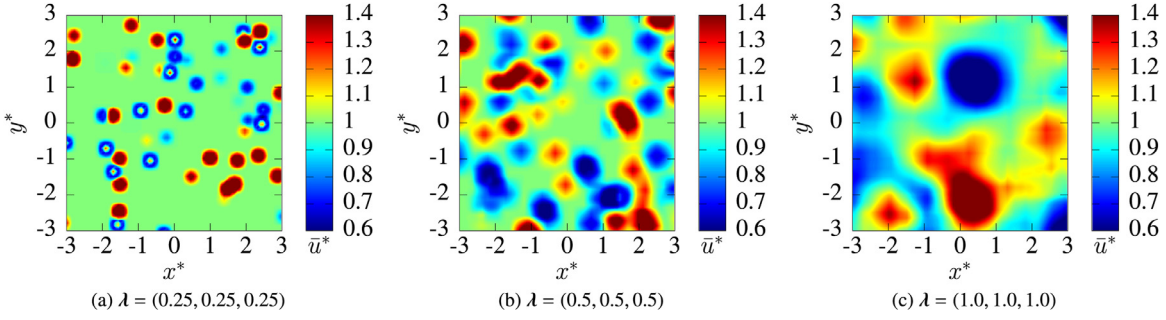

Fig. 7. Example of velocity field provided by the ambient turbulence model for $I_\infty = 15\%$, $N = 1000$ structures of average sizes $\lambda = 0.5$ and increasing variations allowed around this average ($R_f = 2.4$). Slice at $z = 0$ of the 3D reconstructed velocity field of size $6 \times 6 \times 6$.

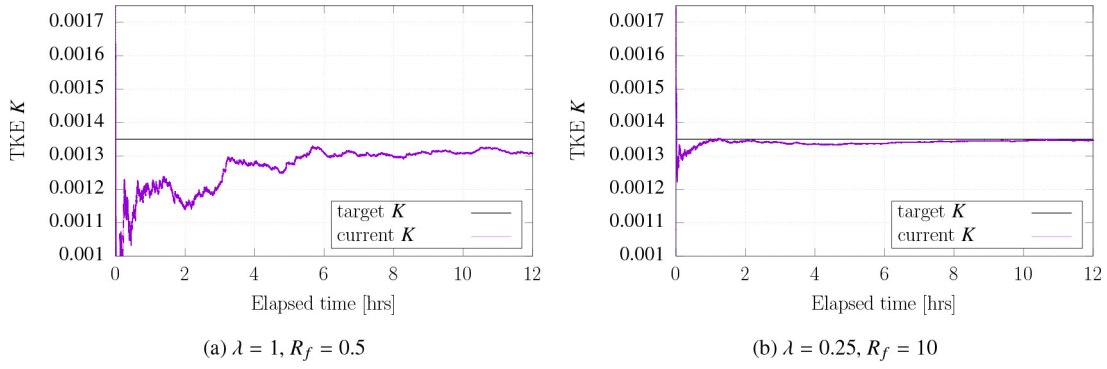

Fig. 8. Time series of the current values of the TKE K computed at a single point over 12 hours of simulated time, for the low turbulence intensity $I_\infty = 3\%$. On the left: an example of very slow convergence, with few turbulent structures of large size λ. On the right: an example of fast convergence, with a high saturation R_f of structures of small size λ.

intensity I_∞ and anisotropic ratio (σ_u:σ_v:σ_w), as their direct link to the Reynolds Stress Tensor is made clear in Eq. (21). It is important to verify the accuracy of this reproduction. In order to simplify this verification, one unique quantity is examined: the Turbulent Kinetic Energy (TKE) K as defined by the following Equation:

$$K = \frac{1}{2}(\sigma_u^2 + \sigma_v^2 + \sigma_w^2). \tag{30}$$

The value of K is calculated based on the velocity time series recorded at a single point in a turbulent flow, as it would be in the context of an experimental study. To this end, a turbulent space $\tilde{E}$ is built around the sampling point. Turbulent structures evolve within this space, advected with the prescribed upstream velocity of $|U^\infty| = 1\ m/s$. Various parameters are tested, such as the size of turbulent structures $\boldsymbol{\lambda}$, the variation on the size of the turbulent structures $\sigma(\lambda)$, and the filling ratio R_f as defined in Eq. (29).

Each time series is generated over a simulated period of 12 hours, with a sampling interval of $dt = 0.1$ seconds. Fig. 8 shows examples of the time series obtained in the "best" and "worse" case scenarios. In the "worse" case, the value of K appears to stabilise eventually at a lower value compared to the target value of 1.35×10^{-3}. As a stochastic method, the

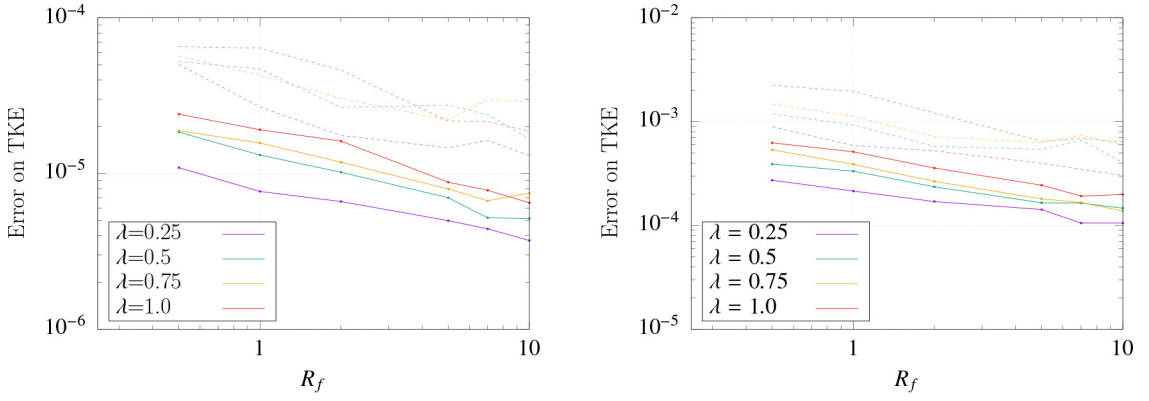

(a) $I_\infty = 3\%$ (b) $I_\infty = 15\%$

Fig. 9. Average error (full lines) and maximal error (dashed lines) on the value of the TKE K plotted against the filling ratio R_f, for various size of turbulent structures $\boldsymbol{\lambda}$. For both the cases of low turbulence intensity (a) and high turbulence intensity (b): $\sigma(\lambda) = 0\%$, and the sub-function f_λ uses the Gaussian kernel.

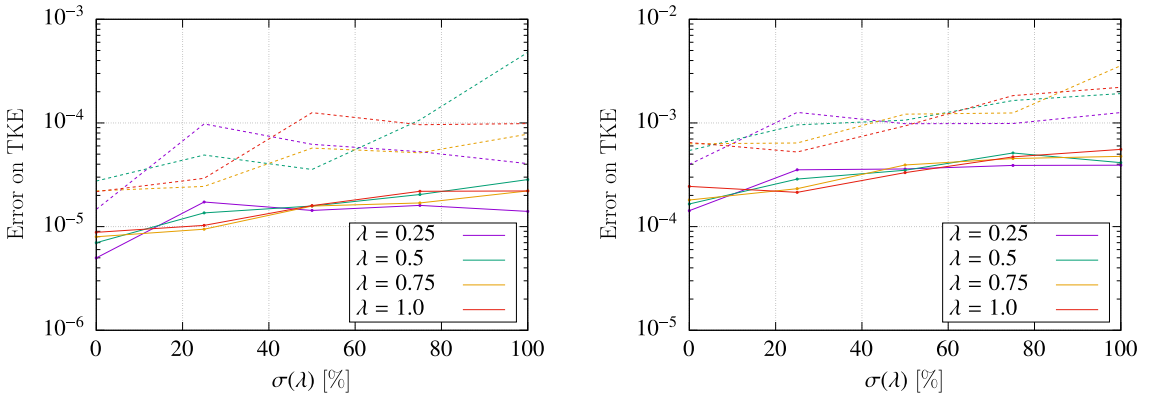

(a) $I_\infty = 3\%$ (b) $I_\infty = 15\%$

Fig. 10. Average error (full lines) and maximal error (dashed lines) on the value of the TKE K plotted against the variance $\sigma(\lambda)$ allowed around average turbulent structure sizes $\boldsymbol{\lambda}$, for various size of turbulent structures $\boldsymbol{\lambda}$. In all cases: $I_\infty = 3\%$, $R_f = 5$, and the sub-function f_λ uses the Gaussian kernel.

SEM is designed so as to ensure an eventual convergence towards this theoretical value. However this convergence is very slow, as there is no evidence of it after 12 hours of simulated time. In this case the filling ratio R_f is low, and since the structures are of larger size λ this means that they are fewer in number. Fewer structures leads to less regeneration of turbulent structures exiting the study space, which causes a slower convergence of the statistical method. Furthermore with the low filling ratio, the sampling point is likely to not be covered by any turbulent structures for a significant part of the time, which explains the lower initial value of K. In the "best" case scenario, the value of K converges and stabilises rapidly at the target value. Due to the probabilistic nature of the Synthetic Eddy Method, these examples of results are not strictly reproducible when repeating the test with the same sets of parameters, but the general tendencies remain.

In order to obtain an accurate representation of the value of K to be expected, 50 time series are computed for each set of parameters. The average and maximal errors on the value of K out of the 50 trials are measured for each set of parameters. Fig. 9 shows the average and maximal errors on the reconstructed TKE for different values of the turbulent structure sizes $\boldsymbol{\lambda}$ and filling ratios R_f. For all structure sizes $\boldsymbol{\lambda}$, the average error on the TKE is at its lowest value for the higher filling ratios R_f. Additionally, the relative position of each average error curve shows that the error on the TKE is lower for smaller structure sizes $\boldsymbol{\lambda}$. Fig. 10 shows the same average and maximal errors on the TKE for different structure sizes $\boldsymbol{\lambda}$, plotted now over a variance $\sigma(\lambda)$ allowed around the average sizes $\boldsymbol{\lambda}$. This graph shows a slight increase in the value of the errors for higher variances $\sigma(\lambda)$. The difference between the curves corresponding to different average sizes $\boldsymbol{\lambda}$ is no longer evident. The blurring of these differences could be explained by the introduction of size variation $\sigma(\lambda)$, meaning that turbulent structures are no longer all of the exact same size $\boldsymbol{\lambda}$ for each curve. In both Figures, the higher and lower turbulent intensity levels show the same general tendencies. The values of the error committed on the TKE are higher for the higher turbulence intensity value $I_\infty = 15\%$. However the value of the TKE is also increased with the higher turbulence intensity, which means that the relative error committed is still comparable.

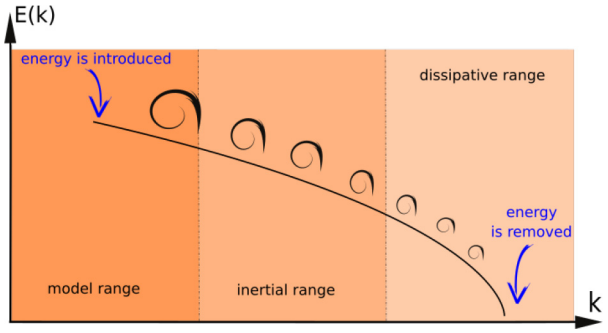

Fig. 11. Diagram of the principle of energetic decay $E(k)$ along the wavenumber k.

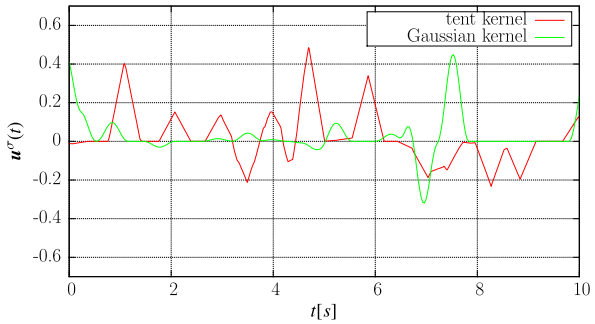

Fig. 12. Temporal measurements of velocity fluctuations $u^\sigma(t)$ at one point, for different kernel functions f_λ (with $I_\infty = 15\%$, $\lambda = 0.25$, $\sigma(\lambda) = 25\%$, $R_f = 1$).

These tests show that for all sets of parameters, the error committed on the value of the TKE is always satisfyingly low compared to the expected values. However it can be concluded that the Reynolds Stress Tensor is more accurately reproduced when using a high number of turbulent structures of small size $\boldsymbol{\lambda}$. Introducing variation on the sizes of the turbulent structures also slightly disrupts its components.

3.2. Physical properties of the flow

In order to pursue the analysis of numerical flows generated by the Synthetic Eddy Method, velocity spectra can also be considered, as is done by Medina [39]. In the following paragraphs, two characteristic physical behaviors of the turbulent flow are analysed. Firstly the time-averaged instantaneous power spectral density (PSD) of the velocity field in the Fourier space illustrates the principle of energy decay in a turbulent flow. Secondly the integral length scale of the flow, also called Taylor macroscale, gives a representation of the size of the generated turbulent structures.

As described in the previous Section, the synthetic turbulence generation method is based on a stochastic algorithm. The statistical properties of turbulent kinetic energy can be described by energy distribution spectra, commonly represented in a logarithmic scale over the wavenumber of the turbulent structures. The concept of energy cascade, as formulated in the work of Richardson and Kolomogorov (see Batchelor [40]), is that kinetic energy enters the turbulent flow at the largest scales to then be transferred to smaller scales, until it is dissipated at the smallest scales by viscous effects. Fig. 11 illustrates this principle.

The purpose of this study is not to measure the kinetic energy along the wavenumber, but rather to paint a picture of the global behaviour of the kinetic energy in the numerically generated turbulent flow. We focus here on the velocity fluctuations at a single central point in the flow, caused by the presence of N generated turbulent structures, as shown in Fig. 12. As expected, the axial velocity variation $u^\sigma(t)$ at this point cycles through unpredictable values in an irregular fashion. These variations are caused by turbulent structures passing successively over the measuring point. Each passing structure causes a velocity fluctuation, the amplitude of which depends on the intensity of the turbulent structure and the distance to its center. Distinctive occurrences of the triangle and Gaussian kernels can be identified, indicating the passage of individual turbulent structures close to the measuring point. These temporal records are used to calculate the spectrum, based on the variations in the driving axis of the flow. Fig. 13 shows the power spectral density for fixed sizes of turbulent structures (i.e. $\sigma(\lambda) = 0\%$), for the four different sub-functions f_λ.

Although the choice of sub-function alters the pattern of the spectrum, the four curves decrease in similar ways. Additionally, it must be noted that the random nature of the stochastic model can cause each of these curves to slightly vary with repeated simulations. While this figure shows the evidence of a general energy decay, this decay is not linear, but

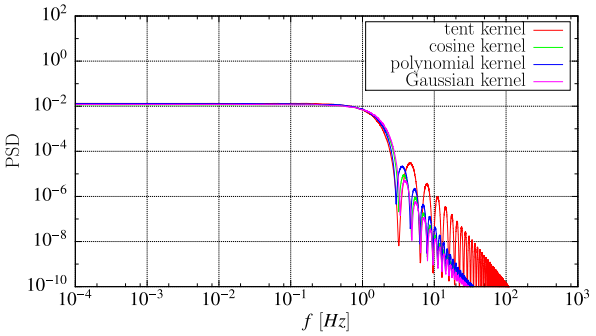

Fig. 13. Power Spectral Distribution : $\lambda = 0.25$, $\sigma(\lambda) = 0\%$.

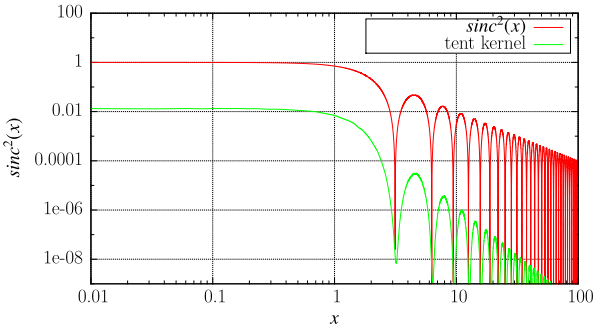

Fig. 14. Comparison between $\text{sinc}^2(x)$ and the same PSD obtained with the tent kernel.

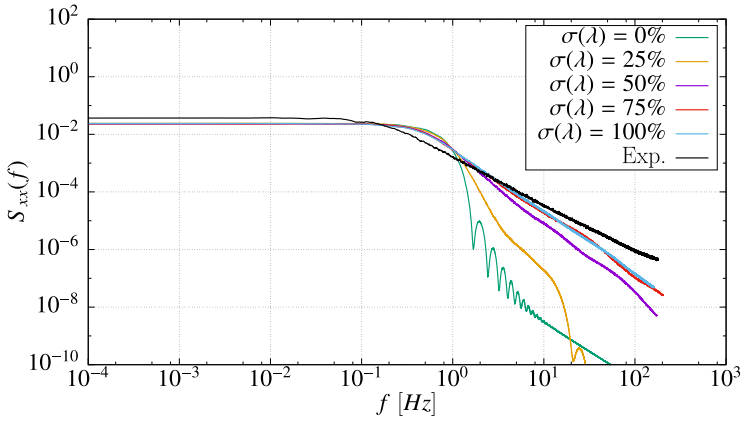

Fig. 15. Influence of $\sigma(\lambda)$ on the spectral representation for a Gaussian kernel ($\lambda = 0.5$ and $R_f = 2$) and comparison with experimental data provided by Medina et al. [41] (for $I_\infty = 15\%$ and $U_\infty = 0.8\ m/s$).

disrupted by recurring “bumps”. These “bumps” can be explained by the nature of the Fourier transform used to compute the PSD. In the simplest case of the triangular kernel, the Fourier transform of a triangle function is a well-known result:

$$\Delta(f) = \mathscr{F}\ (T_{riangle}(t)) = \text{sinc}^2(f). \tag{31}$$

As a sum of triangle functions of identical width λ, the velocity signal is transformed into a sum of proportional square cardinal sinus functions. Fig. 14 verifies the alignment of the square cardinal sinus function with the calculated PSD.

When the standard deviation $\sigma(\lambda)$ on the size of turbulent structures is nonzero, the flow is filled with a range of structures of different sizes. This affects the energy decay represented by the PSD, as shown in Fig. 15. The Fourier transform of the new velocity signal becomes a sum of “bumpy” elements which do not align, leading to a smoother and more realistic curve. This PSD appears to converge with respect to the variation $\sigma(\lambda)$ as of $\sigma(\lambda) = 75\%$, towards a quasi-linear energy decay. The quality of the PSD curves obtained with sufficient variation on the size of the turbulent structures is further validated by comparison with experimental spectra provided by Medina et al. [41]. While the correspondence between numerical and experimental data is not complete, the similarities between these curves is sufficient to conclude that the

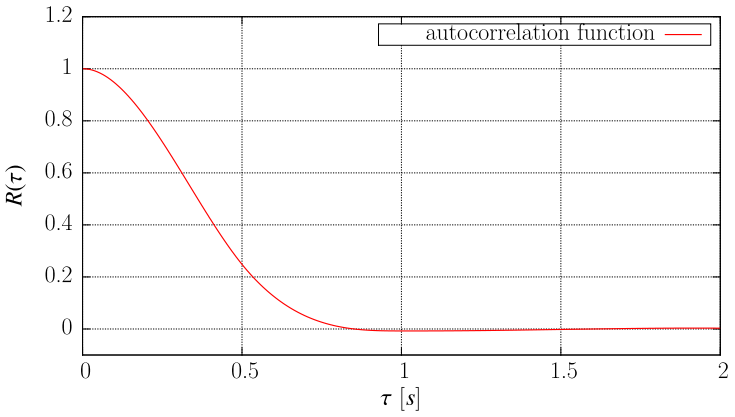

Fig. 16. Sample plot of an autocorrelation function $R(\tau)$ calculated with the numerically generated velocity field.

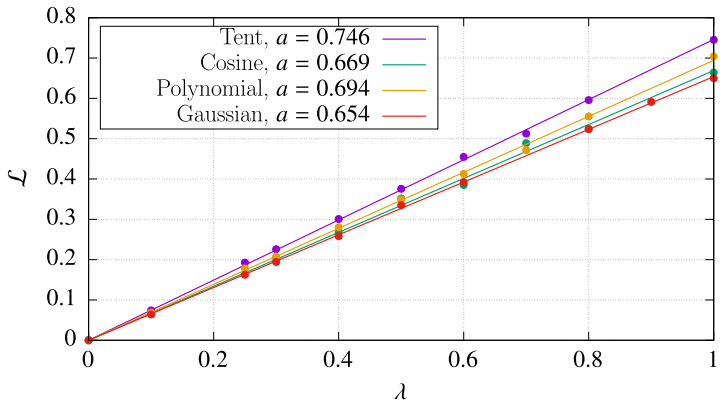

Fig. 17. Linear relation between $\mathscr{L}$ et λ using different kernel functions f_λ.

SEM is capable of accurately representing the energy behaviour of a real turbulent flow. At this point, it is worth remembering that the smaller the variation $\sigma(\lambda)$, the better the convergence of the numerical *TKE* towards the target value (see Fig. 10 above). Therefore, for further applications, a trade-off will have to be made when weighing the importance of both these elements in the choice of the parameter $\sigma(\lambda)$.

True physical turbulent motions occur over a wide range of time and length scales, with the largest scales accounting for the largest transports of momentum and energy. As a second physical analysis of the numerically generated turbulent flows, we attempt to liken the spatial scale of the turbulent behavior to the prescribed sizes λ of the turbulent structures. There are many possible methods to measure the scales of turbulent behavior in a given flow. Among these measures, the Taylor macroscale $\mathscr{L}$ gives an estimate of the characteristic size of turbulent eddies. $\mathscr{L}$ is calculated using the autocorrelation method based once again on the fluid velocity measured at a single point over a period of time:

$$\mathscr{L} = \overline{u} \int_0^\infty R(\tau)\mathrm{d}\tau, \tag{32}$$

with $R(\tau)$ the autocorrelation function. In the present case of a statistically stationary process, the autocorrelation is defined as a function of the time lag τ:

$$R(\tau) = \langle u(t)\ u(t+\tau)\rangle \tag{33}$$

The value of the autocorrelation begins at 1 and then decays with increasing time lag τ, as shown in Fig. 16. As the turbulent velocity fluctuations are randomly generated, the autocorrelation converges towards zero.

The characteristic length $\mathscr{L}$ of the flow is calculated for varying turbulent structure sizes λ, at first with no variance $\sigma(\lambda)$ allowed. The results displayed in Fig. 17 show near-perfect linear relationships obtained between the prescribed sizes λ and the resulting turbulent spatial scales $\mathscr{L}$, for all types of kernel sub-functions f_λ.

The turbulent scales $\mathscr{L}$ are then recalculated with the introduction of variances $\sigma(\lambda)$ around the average structure sizes λ. Table 1 shows that this results in only small disruptions of the value of the scale $\mathscr{L}$. It can thus be assumed that with or without variation on the size λ of the turbulent structures, λ is proportional to the scale of the turbulent behavior in the generated flow.

Table 1
Influence of the variation on the structure sizes $\sigma(\lambda)$ on the value of the Taylor macroscale $\mathscr{L}$ with $R_f = 1$ and the Gaussian kernel.

$\sigma(\lambda)$ (%)	0	25	50	75	100
$\mathscr{L}$ $(\lambda = 0.25)$	0.163	0.163	0.162	0.162	0.169
$\mathscr{L}$ $(\lambda = 0.5)$	0.330	0.336	0.310	0.327	0.328
$\mathscr{L}$ $(\lambda = 0.75)$	0.496	0.478	0.474	0.486	0.518

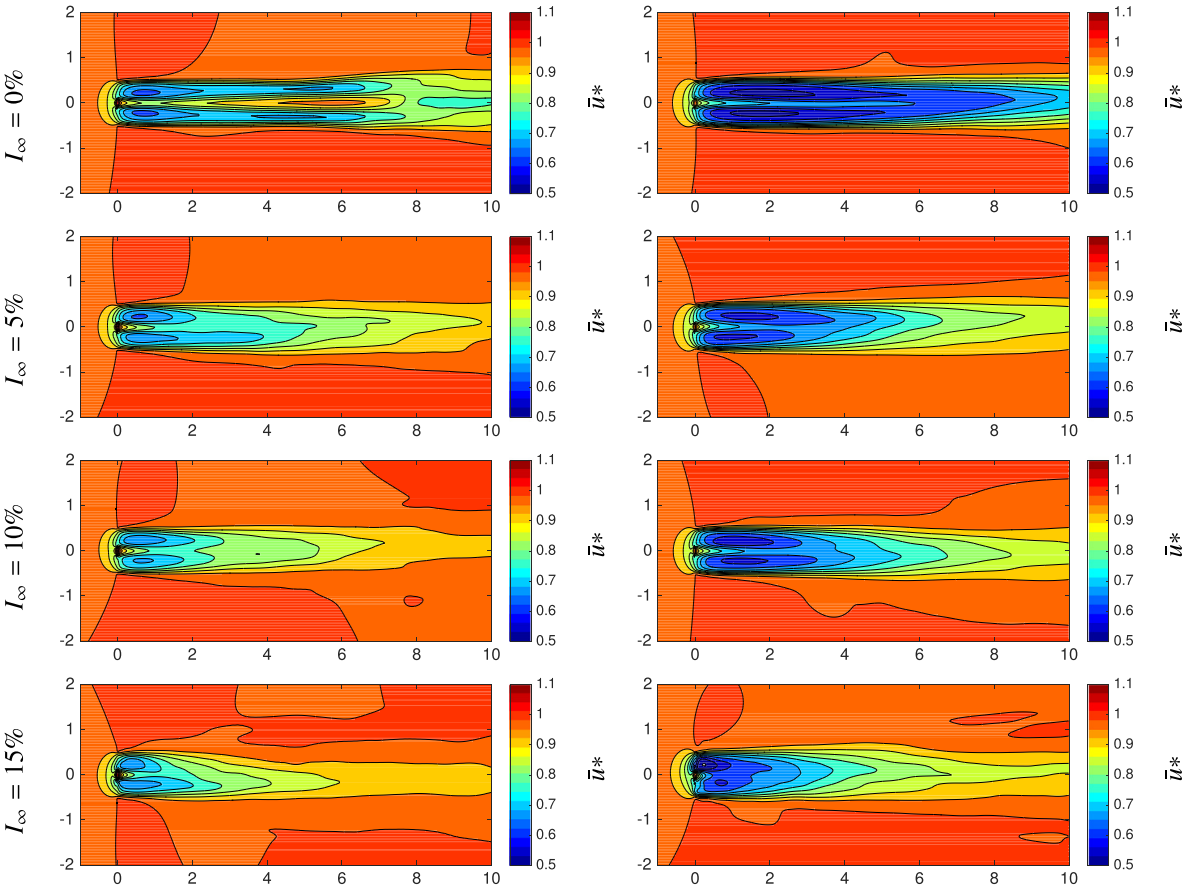

(a) $TSR = 2.5$ (b) $TSR = 3.67$

Fig. 18. Velocity maps in the wake of a single turbine, averaged over a period of 50 to 80 seconds, for varying levels of turbulent intensity. The x and y axis were made dimensionless with respect to the turbine diameter D. $\bar{u}^*$ stands for the dimensionless velocity field and is defined as $|\bar{u}|/U_\infty$.

4. Application to marine current turbine simulation

The properties of turbulent flows generated by the SEM have been thoroughly studied in the absence of turbines. As an illustrative application of the adapted SEM, two simplified turbine simulations are carried out with turbulent intensities I_∞ ranging from 0 to 15%. Though the results are qualitative, they demonstrate the influence of the ambient turbulence created using the adapted SEM throughout the surrounding flow. The aim of this trial is to reproduce the behavior observed in experimental studies, such as Mycek *et. al* [6].

These simulations are carried out with a simplified turbine model: only the three turbine blades are represented. The geometry and specifications of the turbine blades used in these simulations are those of the IFREMER-LOMC turbine model used in [6]. In these computations, in addition to the SEM module presented here, the diffusion model described in Section 2.1 (PSE method using an LES formulation) is used to account for an eddy viscosity affecting the Lagrangian Vortex particles. 90 to 120 seconds of physical time are simulated, and velocity averages are post-treated over the last 50 to 80 seconds once the turbine wake is stabilised. The velocity component $\tilde{u}$ produced by the SEM, as mentioned in Eq. (16), is omitted from this post-treatment, in order to emulate the effect of a longer time average. With a longer time average, this

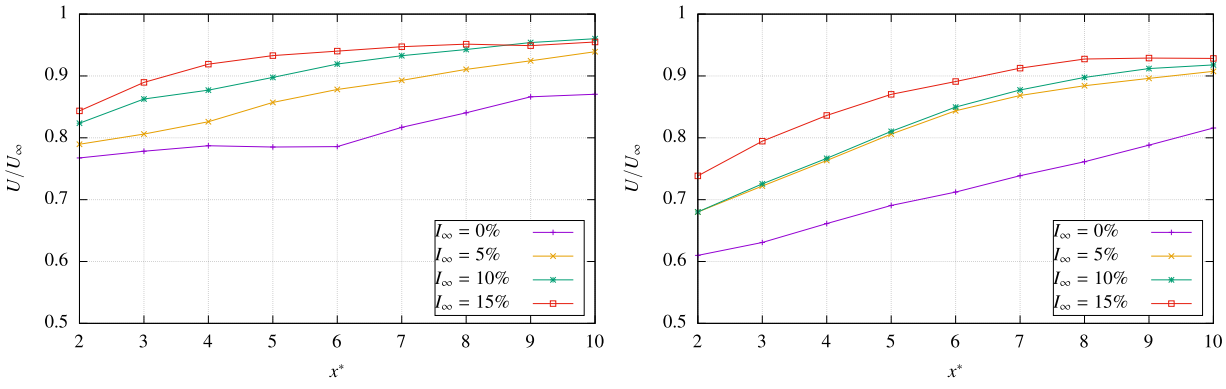

(a) $TSR = 2.5$ (b) $TSR = 3.67$

Fig. 19. Velocity integrated in the wake of a single turbine, on a disc of the same width as the turbine and at given distances downstream of its centre. These curves are produced using the numerical wake velocities shown in map form in the previous Figure.

fluctuating component would even itself out and have no influence on the averaged end result. In all cases, the average upstream velocity remains at $U_\infty = 1\ m/s$ and gravity was neglected. Two turbine rotation speeds are considered, characterized by Tip Speed Ratios $TSR = 2.5$ and $TSR = 3.67$ ($TSR = \frac{\Omega R}{U_\infty}$, with Ω the rotation speed and R the radius of the turbine).

The study space E_S in which the SEM is applied is extended to 1 turbine diameter upstream of the turbine center, 3 diameters above and below, and 12.5 diameters downstream. Experimental data for later comparison is only available up to the cutoff of 10 diameters downstream of the turbine. This allows the wake to be artificially dissipated later on, in order to maximize computational efficiency. The same basic set of SEM parameters is used to obtain the Figures presented hereafter: $\lambda = 0.5$, $\sigma(\lambda) = 0$, and $R_f = 1$.

Fig. 18 shows dimensionless velocity maps of turbine wakes obtained in these conditions for varying turbulent intensities I_∞. Despite the evidence of the missing hub in the form of a heightened velocity at the center of the wake, satisfying tendencies can be observed. First of all, in the absence of ambient turbulence, the turbine wakes extend to approximately 10 diameters downstream of the rotor, which is the correct behaviour expected in low turbulence conditions [42]. Secondly, when using and progressively increasing the ambient turbulence intensity generated by the SEM, the turbine wake becomes progressively shorter. This is further evidenced when considering the velocity deficits integrated in the wake of the turbine. By the relative positioning of the velocity deficit curves, Fig. 19 confirms the ever faster wake recovery as the turbulent intensity is increased. For instance for the case of the lower rotation speed $TSR = 2.5$, the velocity in the wake of the turbine reaches the ratio of 0.9 times the upstream velocity U_∞ at approximately 3.5 diameters downstream of the turbine with the highest turbulence intensity $I_\infty = 15\%$, 7.5 and 5 respectively for turbulence intensities of $I_\infty = 10\%$ and 5%, a value which is not reached within the study space with no turbulence intensity. Computational times were increased by 100 to 200% when using the SEM ambient turbulence generation module with the aforementioned parameters, with respect to the basic case run using no ambient turbulence $I_\infty = 0\%$. For base computational times of approximately 10 hours with 252 cores, the additional CPU cost of this development is not considered to be critical considering the advantages it procures. And a better integration, especially with respect to load balance in the parallel MPI framework, is much probably possible that may drastically diminish this increase.

The Synthetic Eddy Method thus proves its compatibility with the full marine turbine Vortex simulation software. In addition to its ability to reproduce physical properties of experimental flows, it can also have the correct influence on the wake of the turbine, in the form of the shortening of its wake, also observed in experimental studies conducted at IFREMER [6]. It must however be noted that some sets of turbulent parameters may lead to less satisfying results (not presented here): large turbulent structures tend to not have sufficient mixing properties, while small structures may cause important and non physical velocity fluctuations, and a number of any size of turbulent structures can have a strong dissipative effect on the wake regardless of turbulence level.

5. Conclusions and Further work

The Synthetic Eddy Method (SEM) initially proposed by Jarrin et al. [7,8] is successfully adapted to the Lagrangian Vortex framework. The present implementation gives satisfying results regarding the important role played by the ambient turbulence intensity in the behavior of turbine wakes. To the authors' knowledge, this work represents one of the first attempts to account for ambient turbulence in a purely Lagrangian Vortex representation.

The present ambient turbulence model is able to generate a perturbed flow verifying any given turbulence intensity I_∞ and any anisotropic ratio (σ_u:σ_v:σ_w). The study of the Power Spectral Densities (PSD) shows that the introduction of a variation in the sizes of the turbulent structures smoothes the PSD curve of the perturbed flow. This allows for the reproduction of an energy cascade scheme close to experimental measures taken in real turbulent flows. Measuring the Taylor

macroscale in the generated flows shows that the scale of the turbulent behavior depends exclusively on the prescribed turbulent structure sizes. For each considered kernel shape function, there exists a remarkable linear relationship between these two quantities.

As an application example, the compatibility of this method with a Vortex code for the simulation of turbine wakes is verified. The results show that for certain turbulence parameters, the qualitative influence of the turbulent intensity can be accurately reproduced: the turbine wake is dissipated sooner the higher its value.

A limitation of this present implementation of the Synthetic Eddy Method lies in the fact that the added perturbation term is not divergence-free. However for the turbulent intensities considered here, the error introduced in the flow poses no considerable issue. Further work is needed in order to reformulate the velocity perturbation term $\tilde{\boldsymbol{u}}$ in a way that is better compatible with the present Vortex formulation. The divergence-free alternative implementation of the SEM suggested by Poletto et al. [43] is under consideration in the pursuit of this study, as their rotational representation of the perturbation velocity could be better suited to the Lagrangian Vortex framework.

Another avenue of investigation lies in the degree of integration of the perturbation velocity $\tilde{\boldsymbol{u}}$ in the Lagrangian algorithm. In the present implementation, it is only added in the advection step but it could also be integrated into the stretching step or even the diffusion step when using the Diffusion Velocity Method (DVM). This increased integration could be valid for both Jarrin's initial formulation and Poletto's more recent version.

Even in the form of this initial investigation, this new implementation possesses the important advantage over its Eulerian counterparts of allowing the ambient turbulence level to be maintained throughout the entire computational domain, regardless of its size. This is of a crucial importance when considering an array of tidal turbines, to ensure that the same levels of upstream ambient turbulence are perceived by rows of turbines positioned anywhere in the array. This represents a significant step towards the final goal of computing an entire farm of turbines in any realistic operating conditions.

Acknowledgment

The authors acknowledge the financial support the Normandy Regional Council and IFREMER for the funding of Ph.D. grants, as well as the support of the CPER-ERDF programs NEPTUNE and SEMARIN funded by the Normandy Regional Council and the European Union. The present work was performed on computing resources provided by CRIANN (Normandy, France).

References

[1] P. Sagaut, Large Eddy Simulation for Incompressible Flows: an Introduction, Scientific Computation, Springer, 2006.
[2] J. Mansfield, O. Knio, C. Meneveau, Towards lagrangian large vortex simulation, in: ESAIM : Proceedings, Vol. 1, 1996, pp. 49–64.
[3] J. Mansfield, O. Knio, C. Meneveau, A dynamic LES scheme for the vorticity transport equation : formulation and a priori tests, J. Comp. Phys. 145 (Issue 2) (1998) 693–730.
[4] J. Mansfield, O. Knio, C. Meneveau, Dynamic les of colliding vortex rings using a 3d vortex method, J. Comp. Phys. 152 (Issue 1) (1999) 305–345.
[5] I.A. Milne, R.N. Sharma, R.G.J. Flay, S. Bickerton, Characteristics of the turbulence in the flow at a tidal stream power site, Philosophical Transactions of the Royal Society A: Mathematical, Physical and Engineering Sciences 371 (1985) (2013) pp, doi:10.1098/rsta.2012.0196.
[6] P. Mycek, B. Gaurier, G. Germain, G. Pinon, E. Rivoalen, Experimental study of the turbulence intensity effects on marine current turbines behaviour. part I: One single turbine, Renewable Energy 66 (0) (2014) 729–746, doi:10.1016/j.renene.2013.12.036.
[7] N. Jarrin, S. Benhamadouche, D. Laurence, R. Prosser, A synthetic-eddy-method for generating inflow conditions for large-eddy simulations, International Journal of Heat and Fluid Flow 27 (2006) 585–593.
[8] N. Jarrin, Synthetic Inflow boundary conditions for the numerical simulation of turbulence, University of Manchester, 2008 Ph.D. thesis.
[9] I. Afgan, J. McNaughton, S. Rolfo, D. Apsley, T. Stallard, P. Stansby, Turbulent flow and loading on a tidal stream turbine by les and rans, International Journal of Heat and Fluid Flow 43 (2013) 96–108. doi: 10.1016/j.ijheatfluidflow.2013.03.010&domain=pdf
[10] U. Ahmed, I. Afgan, D. Apsley, T. Stallard, P. Stansby, Cfd simulations of full-scale tidal turbine: comparison of les and rans with field data, in: 11th European Wave and Tidal Energy Conference (EWTEC), 2015. Nantes, France
[11] M. Togneri, I. Masters, Parametrising turbulent marine flows for a blade element momentum model of tidal stream turbines, in: 9th European Wave and Tidal Energy Conference (EWTEC), 2011. Southampton, UK
[12] M. Togneri, I. Masters, Synthetic turbulence generation for turbine modelling with BEMT, 3rd Oxford Tidal Energy Workshop, Oxford, UK, 2014.
[13] B.J. Jonkman, L. Kilcher, TurbSim User's Guide: Version 1.06.00, Technical Report, National Renewable Energy Laboratory, 2012.
[14] M.J. Churchfield, Y. Li, P.J. Moriarty, A large-eddy simulation study of wake propagation and power production in an array of tidal-current turbines, Philosophical Transactions of the Royal Society A: Mathematical, Physical and Engineering Sciences 371 (1985) (2013) pp, doi:10.1098/rsta.2012.0421.
[15] M. Togneri, I. Masters, C. Carlier, C. Choma Bex, G. Pinon, Comparison of synthetic turbulence approaches for two numerical tidal turbine models, in: A. Lewis (Ed.), Proceedings of the Twelfth European Wave and Tidal Energy Conference, EWTEC, University College Cork, Ireland, 2017. pp. 765 1–765 10. ISSN: 2309-1983
[16] M. Togneri, C. Carlier, C. Choma Bex, G. Pinon, I. Masters, Comparison of synthetic turbulence approaches for blade element momentum theory prediction of tidal turbine performance and loads, Renewable Energy 145 (2020) 408–418, doi:10.1016/j.renene.2019.05.110.
[17] J. Mann, The spatial structure of neutral atmosphere surface-layer turbulence, Journal of Fluid Mechanics 273 (1994) 141–168.
[18] P. Chatelain, S. Backaert, G. Winckelmans, S. Kern, Large eddy simulation of wind turbine wakes, Flow Turbulence and Combustion 91 (2013) 587–605.
[19] P. Chatelain, M. Duponcheel, S. Zeoli, S. Buffin, D.-G. Caprace, G. Winckelmans, L. Bricteux, Investigation of the effect of inflow turbulence on vertical axis wind turbine wakes, Journal of Physics: Conference Series (Print) 854 (1) (2017) 012011.
[20] P. Degond, S. Mas-Gallic, The weighted particle method for convection-diffusion equations. Part I: The case of an isotropic viscosity, Math. Comp. 53 (188) (1989) 485–507, doi:10.2307/2008716.
[21] J. Choquin, S. Huberson, Particles simulation of viscous flow, Computers & Fluids 17 (2) (1989) 397–410, doi:10.1016/0045-7930(89)90049-2.
[22] G. Cottet, P. Koumoutsakos, Vortex methods: theory and practice, Cambridge University Press, 2000.
[23] Y. Ogami, T. Akamatsu, Viscous flow simulation using the discrete vortex model - the diffusion velocity method, Computers & Fluids 19 (3-4) (1991) 433–441, doi:10.1016/0045-7930(91)90068-S.
[24] P. Mycek, G. Pinon, G. Germain, E. Rivoalen, Formulation and analysis of a diffusion-velocity particle model for transport-dispersion equations, Computational and Applied Mathematics 35 (2) (2016) 447–473, doi:10.1007/s40314-014-0200-5.
[25] C. Rehbach, Calcul numrique d'coulements tridimensionnels instationnaires avec nappes tourbillonaires, La Recherche Arospatiale 5 (1977) 289–298.
[26] R. Lewis, Vortex element methods for fluid dynamic analysis of engineering systems, Cambridge University Press, 1991.

[27] G. Pinon, P. Mycek, G. Germain, E. Rivoalen, Numerical simulation of the wake of marine current turbines with a particle method, Renewable Energy 46 (0) (2012) 111–126, doi:10.1016/j.renene.2012.03.037.
[28] A. Leonard, Vortex methods for flow simulation, Journal of Computational Physics 37 (3) (1980) 289–335, doi:10.1016/0021-9991(80)90040-6.
[29] G.S. Winckelmans, A. Leonard, Contributions to vortex particle methods for the computation of three-dimensional incompressible unsteady flows, Journal of Computational Physics 109 (2) (1993) 247–273, doi:10.1006/jcph.1993.1216.
[30] K. Lindsay, R. Krasny, A particle method and adaptive treecode for vortex sheet motion in three-dimensional flow, J. Comput. Phys. 172 (2001) 879–907.
[31] G. Pinon, H. Bratec, S. Huberson, G. Pignot, E. Rivoalen, Vortex method for simulation of a 3D round jet in a cross-stream, Journal of Turbulence 6 (18) (2005) 1–25.
[32] F. Hauville, Y. Roux, Réglage dynamique d'une voile par une méthode d'intraction fluide/structure, 9èmes Journes de l'Hydrodynamique, Publisher, 2003.
[33] M. Luersen, R. Le Riche, D. Lemosse, O. Le Maître, A computationally efficient approach to swimming monofin optimization, Structural and Multidisciplinary Optimization 31 (6) (2006) 488–496, doi:10.1007/s00158-006-0001-6. (9)
[34] C. Carlier, G. Pinon, B. Gaurier, G. Germain, E. Rivoalen, Numerical and experimental study of elementary interactions in marine current turbines array, in: 10th European Wave and Tidal Energy Conference (EWTEC), 2015. Nantes, France
[35] P. Mycek, G. Pinon, C. Lothodé, A. Dezotti, C. Carlier, Iterative solver approach for turbine interactions: application to wind or marine current turbine farms, Applied Mathematical Modelling 41 (2017) 331–349, doi:10.1016/j.apm.2016.08.027.
[36] J.R. Mansfield, O.M. Knio, C. Meneveau, Dynamic les of colliding vortex rings using a 3d vortex method, Journal of Computational Physics 152 (1) (1999) 305–345, doi:10.1006/jcph.1999.6258.
[37] N. Mansour, J. Ferziger, W. Reynolds, Large-eddy simulation of a turbulent mixing layer, Technical Report, Report TF-11, Thermosciences Div., Dept. of Mech. Eng., Stanford University, 1978.
[38] T.S. Lund, X. Wu, K.D. Squires, Generation of turbulent inflow data for spatially-developing boundary layer simulations, Journal of Computational Physics 140 (1998) 233–258.
[39] O.D. Medina, F. Schmitt, R. Calif, G. Germain, B. Gaurier, Correlation between synchronised power and flow measurements, a way to characterize turblence effecs on marine current turbine., in: 11th European Wave and Tidal Energy Conference (EWTEC), 2015. Nante, France
[40] G.K. Batchelor, The Theory of Homogeneous Turbulence, Cambridge University Press, 1953.
[41] O.D. Medina, F.G. Schmitt, R. Calif, G. Germain, B. Gaurier, Turbulence analysis and multiscale correlations between synchronized flow velocity and marine turbine power production, Renewable Energy 112 (2017) 314–327, doi:10.1016/j.renene.2017.05.024.
[42] C. Carlier, G. Pinon, B. Gaurier, G. Germain, E. Rivoalen, A synthetic eddy-method to represent the ambient turbulence in numerical simulation of marine current turbine, in: 10th European Wave and Tidal Energy Conference (EWTEC), 2015. Nantes, France
[43] R. Poletto, T. Craft, A. Revell, A new divergence free synthetic eddy method for the reproduction of inlet flow conditions for les, Flow, Turb. and Combustion 91 (2013) 519–539.